Energy &
Environmental
Science

PAPER

Cite this: *Energy Environ. Sci.*, 2025, **18**, 8838

A weakly solvating solvent-based quasi-solid electrolyte for sodium metal batteries

Ho Mei Law,†[ab] Zilong Wang,†[c] Shengjun Xu,[ab] Longyun Shen,[d] Baptiste Py,[c] Yuhao Wang,[c] Renée Siegel,[e] Jürgen Senker,[be] Qingsong Wang*[bf] and Francesco Ciucci*[ab]

Received 17th April 2025,
Accepted 13th August 2025

DOI: 10.1039/d5ee02153g

rsc.li/ees

Sodium-ion batteries represent a more sustainable and, potentially, cost-effective alternative to lithium-ion technology, with sodium–metal anodes showing promise for achieving high-energy densities. However, the strong reactivity between sodium–metal and conventional liquid electrolytes leads to unstable solid electrolyte interphases, undermining battery performance and safety. To address this challenge, this work introduces a novel weakly solvating quasi-solid electrolyte. This electrolyte is fabricated *via in situ* polymerization of polyethylene glycol diacrylate with sodium bis(fluorosulfonyl)imide in a mixed solvent system of 2-methyltetrahydrofuran and cyclopentyl methyl ether, which enables targeted manipulation of the solvation of the sodium cation. Computational and spectroscopic analyses reveal that this design promotes anion-dominated solvation, facilitates the formation of a robust anion-derived solid electrolyte interphase, suppresses dendrite formation, and enhances stability and cell performance. Batteries using this weakly solvating solvent-based quasi-solid electrolyte achieve an average coulombic efficiency of 98.4% over 400 cycles (at 0.5 mA cm^{-2}, 0.5 mAh cm^{-2} in half-cell tests) and retain a capacity of 1077 mAh g^{-1} (based on sulfur content) over 250 cycles when paired with sulfurized polyacrylonitrile cathodes. These findings establish a new paradigm for developing practical, high-performance sodium–metal batteries.

Broader context

Sodium–metal batteries (NMBs) are rapidly emerging as a promising alternative for next-generation energy storage due to the abundance of sodium, high theoretical capacity, and cost advantages over lithium-ion batteries. However, the practical implementation of NMBs faces a critical challenge: the formation of unstable solid electrolyte interphases (SEIs) at the sodium metal surface. While numerous strategies have been developed to address this issue, most are limited by increased cost, environmental concerns, or safety risks. Here, we propose a transformative approach to electrolyte design by introducing the concept of ''weakly solvating solvent-based quasi-solid electrolytes'', which simultaneously addresses several fundamental challenges. By integrating weakly solvating solvents (MTHF and CPME) *in situ* into a polymerized PEGDA matrix, we fundamentally alter the sodium ion solvation structures to promote anion-dominated coordination environments. This molecular-level strategy yields remarkable electrochemical performance in batteries when paired with sulfurized polyacrylonitrile cells, maintaining high capacity (1077 mAh g^{-1}) after 250 cycles. Our approach represents a comprehensive solution that combines the safety benefits of quasi-solid systems with the performance advantages of controlled solvation chemistry, potentially accelerating the practical deployment of sodium-based energy storage for large-scale applications.

Introduction

Sodium (Na)–metal batteries (NMBs) are emerging as a promising alternative to lithium-ion batteries due to the abundance of Na, its high theoretical capacity (1166 mAh g^{-1}), low electrochemical potential (−2.71 V *vs.* the standard hydrogen electrode), and low projected cost.[1–4] Despite these advantages, their development is hindered by the challenges posed by Na-metal anodes when paired with conventional liquid electrolytes (LEs), which lead to the formation of unstable solid electrolyte interphases (SEIs).[5,6] The repeated destruction and

---

[a] *Chair of Electrode Design for Electrochemical Energy Systems, University of Bayreuth, Weiherstraße 26, 95448 Bayreuth, Bavaria, Germany. E-mail: francesco.ciucci@uni-bayreuth.de*
[b] *Bavarian Center for Battery Technology (BayBatt), University of Bayreuth, Universitätsstraße 30, 95447 Bayreuth, Germany*
[c] *Department of Mechanical and Aerospace Engineering, The Hong Kong University of Science and Technology, Clear Water Bay, Kowloon, Hong Kong SAR, China*
[d] *Division of Emerging Interdisciplinary Areas, The Hong Kong University of Science and Technology, Clear Water Bay, Hong Kong SAR, P. R. China*
[e] *Department of Chemistry, Inorganic Chemistry III, and Northern Bavarian NMR Centre, University of Bayreuth, Universitätsstraße 30, Bayreuth 95440, Germany*
[f] *Department of Chemistry, University of Bayreuth, Universitätsstraße 30, 95447 Bayreuth, Germany. E-mail: Qingsong.Wang@uni-bayreuth.de*

† These authors contributed equally to this work.

reconstruction of these SEIs during electrochemical cycling results in decreased coulombic efficiency (CE), rapid performance decline, and dendrite formation. Research efforts to achieve stable Na–metal have primarily focused on building robust SEIs through electrolyte engineering.[5,7–10] Key strategies have included introducing additives[11–13] and salts,[8,14] varying salt concentrations,[15,16] or using fluorinated solvents.[13,17,18] These strategies aim to create an inorganic-rich SEI on Na–metal that mechanically inhibits dendrite growth by either controlled decomposition of additives or salts or enhanced Na$^+$–anion pairing, resulting in improved electrochemical performance.[19,20] Despite their potential, these methods face practical challenges, such as high costs, elevated viscosity due to increased salt concentrations, and potential toxicity and sustainability issues.[21–23]

Recent advances in weakly solvating electrolytes (WSEs) provide an alternative approach that significantly improves battery performance by promoting the formation of inorganic-rich SEIs.[7,24–27] Conventional LEs use strongly solvating solvents that readily dissolve Na salts, facilitating the creation of abundant solvent-separated ion pairs (SSIPs, where one or more solvent molecules completely separate the Na$^+$). These strong Na$^+$–solvent interactions lead to the formation of mechanically weak, solvent-derived SEI on Na–metal with poor stability, as illustrated in Fig. 1. In contrast, WSEs use weakly solvating solvents that intentionally limit salt dissolution, thereby reducing Na$^+$–solvent interactions while maximizing Na$^+$–anion interactions.[24,28] This alteration in solvation structure creates an anion-rich environment around Na$^+$, even at moderate salt concentrations (in the order of 2 M).[7,29] Consequently, the inorganic-rich anions (*e.g.*, bis(fluorosulfonyl)imide (FSI$^-$) from sodium bis(fluorosulfonyl)imide (NaFSI)) form anion-derived SEIs that are inherently stable, resulting in longer cycling life and improved rate capabilities.[20,24] For example, including cyclopentyl methyl ether (CPME) in lithium batteries and 2-methyltetrahydrofuran (MTHF) in NMBs as a weakly solvating solvent has led to average CEs of 99.3% over 350 cycles[30] and 99.6% over 100 cycles,[18] respectively. While MTHF has been validated in Na systems, CPME, despite its proven effectiveness in lithium batteries, remains virtually unexplored in NMB applications. Additionally, these liquid-based WSEs still face fundamental safety concerns related to flammability and leakage.[3,8,31–33]

Quasi-solid electrolytes (QSEs) address the limitations of LEs through a safer polymer matrix structure.[32–34] Comprising a polymer matrix, Na salts, and solvents, QSEs achieve ionic conductivities of 1 to 5 mS cm^{-1} at room temperature[35,36] that are comparable to those of LEs. The *in situ* polymerization process used to create QSEs enhances electrode–electrolyte contact and, relative to solid-state electrolytes, reduces interfacial resistances, thus improving battery performance.[32,37,38] Various polymers, such as pentaerythritol triacrylate,[39] poly(ethylene glycol) diacrylate (PEGDA),[33] poly(butyl acrylate),[34] poly(vinylene carbonate),[40] and poly(1,3-dioxolane),[41] have been successfully utilized in *in situ* polymerized QSEs for NMBs, demonstrating promising results. Notably, PEGDA-based QSEs have exhibited exceptional Na metal stability over 2000 hours at 0.1 mA cm^{-2}, attributed to the presence of carbonyl groups ($\mathrm{C{=}O}$), which modify the Na$^+$ solvation structure.[33] Despite these advances, current QSE systems for NMBs still employ conventional strongly solvating electrolytes,[32–34,41] leading to solvent-derived SEIs.

This work introduces a strategy for controlling the Na$^+$ solvation structure in the QSE through the integration of weakly solvating solvents into the polymer matrix. Our innovation centers on two key points. First, we developed a novel QSE system using *in situ* free radical polymerization of a liquid precursor, which combines 2 M of NaFSI in MTHF with PEGDA as the crosslinking agent. The $\mathrm{C{=}O}$ groups in the PEGDA network weaken Na$^+$–solvent interactions, shifting Na$^+$ coordination toward anions. Second, we enhance this solvation structure by incorporating CPME, a weakly solvating co-solvent that has been previously unexplored in NMBs or QSE applications.[30,42] This combination creates a weakly solvating solvent-based QSE (WS-QSE) that promotes the formation of anion-rich Na$^+$ complexes, including contact ion pairs (CIPs, where an anion coordinates to a single Na$^+$) and aggregate ion pairs (AIPs, where an anion coordinates to two or more Na$^+$), and results in an anion-dominated Na$^+$ solvation structure. In turn, this controlled solvation environment facilitates the formation of a stable, anion-derived SEI on the Na–metal surface through the reductive decomposition, as illustrated in Fig. 1.

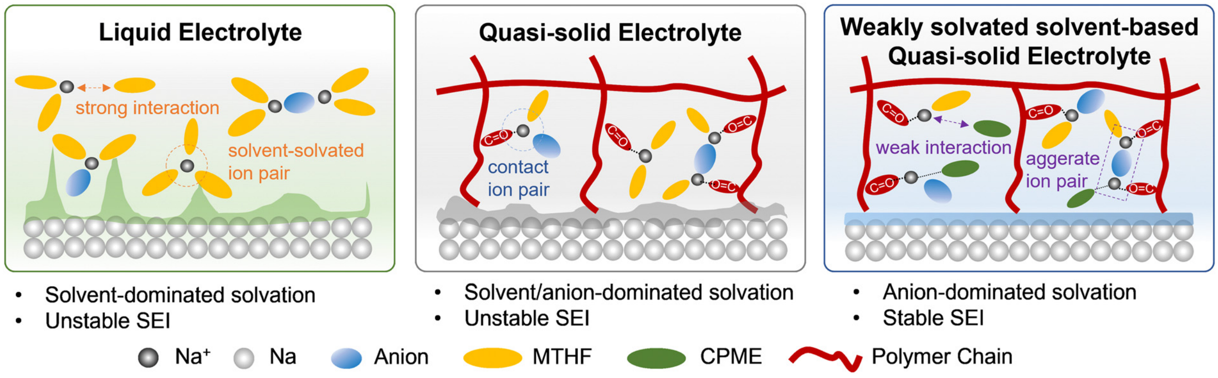

Fig. 1 Schematic diagrams of Na–metal anodes displaying different SEI compositions: solvent-derived SEI using LE (left), solvent/anion-derived SEI using QSE (middle), and anion-derived SEI using WS-QSE (right).

Electrochemical performance tests confirmed the effectiveness of the system. In Na|carbon-coated aluminum (Al) half-cell tests, the WS-QSE achieved an impressive average CE of 98.4% (at 0.5 mA cm^{-2}, 0.5 mAh cm^{-2}) over 400 cycles. We also evaluated WS-QSE with a sulfurized polyacrylonitrile (SPAN) cathode, which was selected for its high theoretical capacity (1675 mAh g^{-1}) and structural stability due to the presence of covalent sulfur-polyacrylonitrile bonds.[13,43,44] The Na|WS-QSE|SPAN system showed remarkable cycling stability (all capacities based on sulfur content unless indicated otherwise), retaining a specific capacity of 1077 mAh g^{-1} (484.7 mAh g$_{\text{SPAN}}{}^{-1}$) after 250 cycles at 240 mA g^{-1} or 0.32 mA cm^{-2}. Even with an increased areal capacity of 2.3 mAh cm^{-2}, the battery could retain 1099 mAh g^{-1} (494.6 mAh g$_{\text{SPAN}}{}^{-1}$) over 150 cycles at 120 mA g^{-1} (0.25 mA cm^{-2}). In short, this work develops a novel electrolyte design in NMBs, contributing to both a fundamental understanding of ion solvation behavior in QSEs and the practical development of next-generation energy storage systems.

Results and discussions

Electrolyte design

Effective electrolyte design hinges on controlling solvent-ion interactions by manipulating three key molecular-level properties: coordination capacity (the number of oxygen atoms), steric hindrance (bulky substituents that restrict access to Na$^+$), and chelation ability (multiple binding sites for Na$^+$ on a single molecule). These properties collectively determine solvating power, thereby impacting ion transport, interfacial chemistry, and electrochemical stability.[18,24,45,46] Five-membered ring ethers (*e.g.*, tetrahydrofuran and MTHF) and six-membered ring ethers (*e.g.*, tetrahydropyran) create steric hindrance to weaken Na$^+$–solvent interactions, which promote Na$^+$–anion pairing and stable inorganic-rich SEI formation.[18,21,27] MTHF exhibits the strongest Na$^+$–anion pairing due to methyl substitution, but still shows long-term cycling limitations.[18]

To improve performance through molecular design, we chose two structurally similar cyclic ether-based solvents, MTHF and CPME. While both molecules contain a five-membered ring with an oxygen atom, they exhibit significant differences in their molecular structures. As shown in Fig. 2a, CPME features a bulky cyclopentyl ring connected to oxygen through a methyl bridge, which creates a greater steric hindrance and consequently solvates Na$^+$ more weakly than MTHF. This difference in solvating ability is quantitatively supported by the dielectric constants (ε), which indicate an ability to dissociate ion pairs.[10,24,47] CPME exhibits a lower value (ε = 4.7)[30] than MTHF (ε = 6.97)[26] (Fig. 2a and Table S1 in the SI). Dipole moments (μ, Table S1) further confirm this trend, with CPME showing a lower value (μ = 1.27 D) than MTHF (μ = 1.38 D). Both cyclic ethers demonstrate weaker solvation properties than the conventional linear ether-based solvent 1,2-dimethoxyethane (DME, ε = 7.2,[24] μ = 1.71 D, Table S1), making them promising candidates for our weakly solvating solvent strategy.

Density functional theory (DFT) calculations revealed the specific electronic interactions between Na$^+$ and the solvent molecules, providing molecular-level insights into their coordination behavior. Fig. S1 displays negative charge densities at the oxygen atoms of both MTHF and CPME in the electrostatic potential analysis, indicating that these oxygen atoms are preferential binding sites for Na$^+$. However, CPME showed a lower negative electron density (−1.17 eV) at the oxygen atom compared to MTHF (−1.3 eV) (Fig. S1), suggesting weaker Na$^+$–CPME interactions. Binding energy calculations, which quantify the thermodynamic stability of Na$^+$–solvent complexes, further support these findings. As illustrated in Fig. 2b, the Na$^+$–MTHF complex exhibits a higher negative binding energy (−1.41 eV) than Na$^+$–CPME (−1.36 eV). These computational results align well with experimental observations: pure CPME cannot dissolve NaFSI at a 0.5 M concentration (Fig. S2a), while a MTHF/CPME mixture (50 : 50, volume ratio) successfully dissolves NaFSI up to a 2.0 M concentration (Fig. S2b). Based on these results, we chose MTHF as the primary solvent for NaFSI dissociation, with CPME acting as a co-solvent to modulate the Na$^+$ solvation structure due to its lower solvation power.

For the polymer component selection, we identified PEGDA as the optimal crosslinking agent due to its exceptional networking-forming capabilities,[33,48] which facilitated the formation of a polymer network. Through thermally initiated free-radical *in situ* polymerization of the LE (2.0 M NaFSI in MTHF) with PEGDA, as discussed in Fig. S3 and the Methods section in the SI, we obtained a QSE with solid-like polymer characteristics after evaluating several candidate monomers (Fig. S4 and SI I). In addition to structural benefits, the carbonyl groups (C═O) in PEGDA play a critical role in manipulating the Na$^+$ solvation structure.[33,49] The presence of C═O groups weakens Na$^+$–solvent bonds[33,34,49] reducing the formation of SSIPs (Fig. 1). To further promote an anion-dominated solvation structure, we incorporated CPME as a weakly solvating co-solvent (MTHF : CPME = 50 : 50 vol%) in the liquid precursor. This formulation, which we designate as WS-QSE, combines PEGDA's carbonyl interactions with CPME's inherently weak solvating properties to create an environment that favors CIPs and AIPs, significantly enhancing the stability of the resulting SEI layer (Fig. 1).

We used molecular dynamics (MD) simulations (Fig. 2c–e) to investigate the Na$^+$ solvation environment in the WS-QSE and validate our design principles. Using the local minimum (2.9 Å) in the radial distribution function (RDF) as the shell boundary,[37] we calculated coordination numbers (CNs) for various Na$^+$–molecule interactions (Fig. 2f). These CNs quantify the number of solvent molecules or anions surrounding each Na$^+$ and provide direct evidence for solvation structure. The simulations revealed distinct patterns of anion coordination: the CNs of Na$^+$–O$_{\text{FSI}}{}^-$ were 3.75, 3.75, and 4 for WS-QSE, QSE, and LE, respectively. In contrast, the CNs of Na$^+$–solvent (encompassing both Na$^+$–O$_{\text{MTHF}}$ and Na$^+$–O$_{\text{CPME}}$ interactions), showing an inverse relationship: 0.31 for WS-QSE, 0.36 for QSE, and 1.5 for LE. This significant reduction in solvent coordination, while maintaining similar anion coordination, indicates a predominantly anion-dominated solvation environment in both QSE systems, with WS-QSE showing the most pronounced effect. The

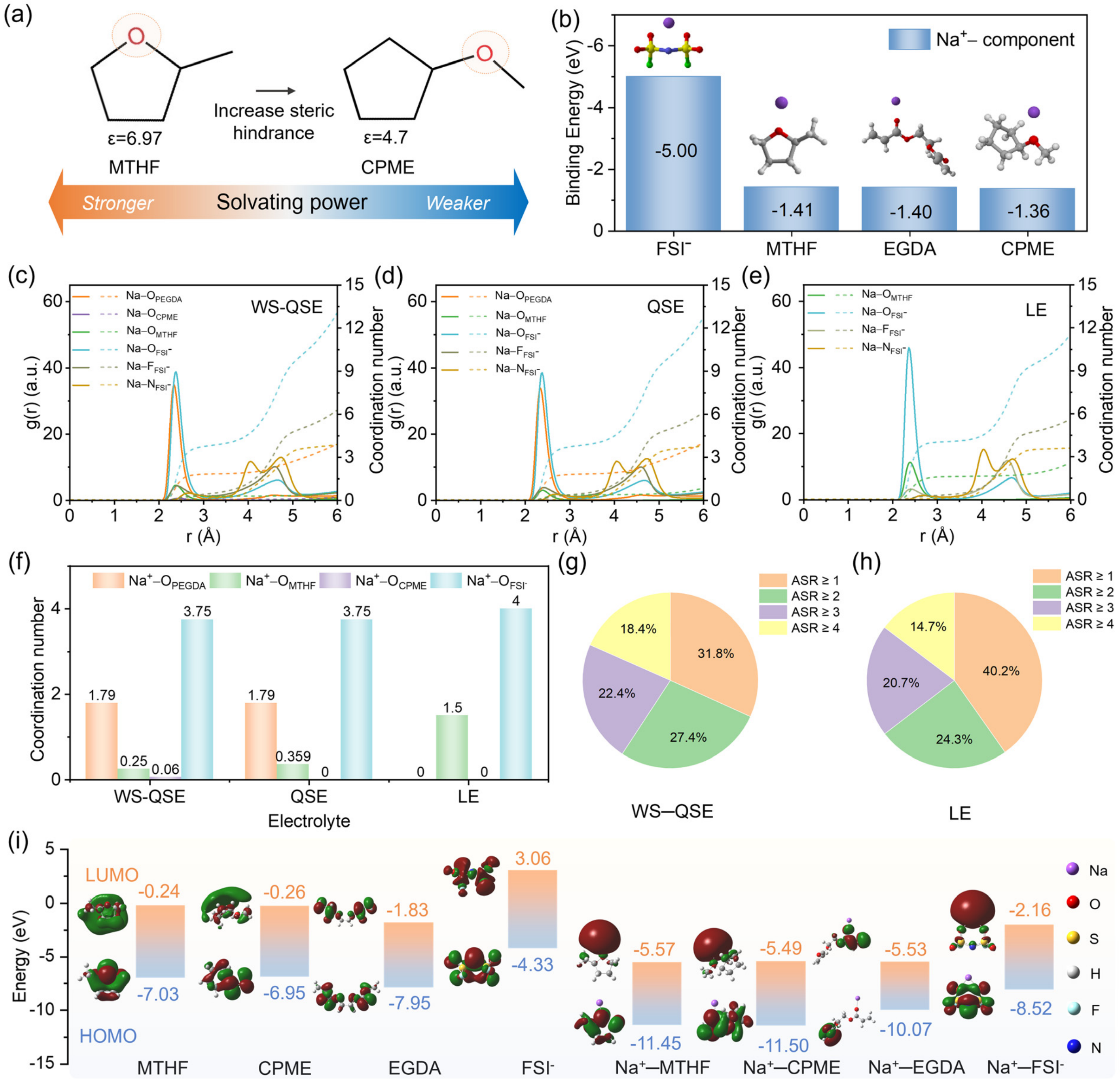

Fig. 2 (a) Molecular structure of MTHF and CPME with an illustration of solvating power. (b) Binding energies of Na^+–FSI^-, Na^+–MTHF, Na^+–ethylene glycol diacrylate (EGDA), and Na^+–CPME. RDF and CNs calculated from MD simulations (c) WS-QSE, (d) QSE, and (e) LE. (f) CN analysis for WS-QSE, QSE, and LE. Anion-to-solvent ratio of (g) WS-QSE and (h) LE. (i) HOMO/LUMO obtained from DFT calculations of various components and their Na^+ complexes.

anion-to-solvent ratio (ASR) was used to compare solvation structures (Fig. 2g, h and Fig. S5).[50,51] WS-QSE achieved the highest distribution of ASR ≥ 4 (18.4%), exceeding both QSE (17.6%) and LE (14.7%). This improved ratio can be attributed to the synergistic effects of adding PEGDA and CPME. While the LE showed high CNs of Na^+–$O_{FSI}{}^-$, its substantial solvent binding resulted in an overall lower ASR ≥ 4. These computational findings provide preliminary evidence for an anion-dominated solvation structure in WS-QSE.

Informed by these solvation environment findings, we then analyzed the molecular orbital energy levels to evaluate the electrochemical stability of the different coordination configurations. The lowest unoccupied molecular orbital (LUMO) levels were calculated since they affect SEI formation, while the highest occupied molecular orbital (HOMO) levels influence oxidation stability at the cathode. As shown in Fig. 2i, the LUMO energies of MTHF (−0.24 eV) and CPME (−0.26 eV) are nearly identical, indicating comparable electrochemical stability. However, upon Na^+ coordination, their complexes exhibited significantly lower LUMO levels: −5.57 eV for Na^+–MTHF and −5.49 eV for Na^+–CPME. According to the literature,[52] this decrease in LUMO energies results from orbital hybridization between Na atomic orbitals and solvent molecular orbitals, leading to lower energy states that promote C–O bond cleavage and subsequent decomposition. Consequently, these coordinated complexes decompose more readily, resulting in less stable, organic solvent-derived SEIs.[27] In contrast, the Na^+–FSI^- complexes display a much lower LUMO level (−2.16 eV) compared to the bare FSI^- anion (3.06 eV). This notable energy difference suggests that Na^+–FSI^- complexes are more susceptible to reduction than the free FSI^- anion, facilitating the formation of robust, inorganic-derived SEIs on the Na–metal surface. Thus, manipulating an anion-dominated solvation structure in the electrolyte promotes the formation of more stable, anion-derived SEIs.[27]

Physicochemical properties of the WS-QSE

Following our systematic electrolyte design approach, we conducted a comprehensive set of physicochemical characterizations for both QSE and WS-QSE systems to verify their structural properties and thermal stability. The successful polymerization of QSE and WS-QSE is illustrated in Fig. 3a and b, respectively, and was confirmed through several analytical techniques. Attenuated total reflection Fourier transform infrared spectroscopy (ATR-FTIR) demonstrated complete polymerization by showing the disappearance of C═C peaks at 1407 cm^{-1} (Fig. 3c). Complementary Raman spectroscopy further confirmed the absence of C═C bonds, with peaks at 1401 and 1633 cm^{-1} (Fig. 3d). Thermogravimetric analysis (TGA) indicated enhanced thermal stability in both the QSE and WS-QSE systems, with the temperature for 10% weight loss ($T_{10\% \text{ loss}}$) reaching approximately 150 °C, which is significantly higher than that of the LE (94 °C, Fig. S6). This enhancement can be attributed to the heat resistance of the cross-linked PEGDA polymer backbone.[48]

We used a suite of spectroscopic techniques to investigate the anion-dominated Na^+ solvation structure in WS-QSE. Raman spectroscopy of the S–N–S stretching of FSI^- (720 to 750 cm^{-1}) revealed that CIPs and AIPs account for the majority (>70%) of the species in all electrolyte systems (Fig. 3d, e and Fig. S7). Raman spectroscopy revealed significant differences in AIP content across electrolyte systems, with WS-QSE containing the highest proportion (22%) compared to QSE (14%) and LE (11%) (Fig. S7), as evidenced by the characteristic peak shifts shown in Fig. 3e. This enhancement resulted from two synergistic effects: the strong Na^+ binding to the polymer backbone, as evidenced by the shift of the C═O peak of PEGDA from 1720 to 1727 cm^{-1} (Fig. 3c and d), and the reduced solvating power of CPME. These factors effectively reduced SSIPs from 17% in LE to only 4% in WS-QSE (Fig. 3e and Fig. S7), indicating the successful establishment of an anion-dominated Na^+ solvation structure.

To validate our Raman spectroscopy findings with complementary analytical evidence, we employed magic-angle spinning (MAS) solid-state nuclear magnetic resonance (NMR) spectroscopy, providing direct molecular-level insights into the Na^+ solvation environments. As shown in Fig. 3f and Fig. S8a, the ^{23}Na MAS spectra displayed progressive upfield shifts from LE (−7.1 ppm) to QSE (−10.4 ppm) and to WS-QSE (−12.8 ppm). This trend indicates increasing electron shielding around Na^+, with the enhanced shielding attributed to PEGDA incorporation, which expands the first coordination shell for QSE and WS-QSE. A similar shift (−11.4 ppm) was observed for the ^{23}Na resonance of crystalline NaFSI (Fig. S8a), where the

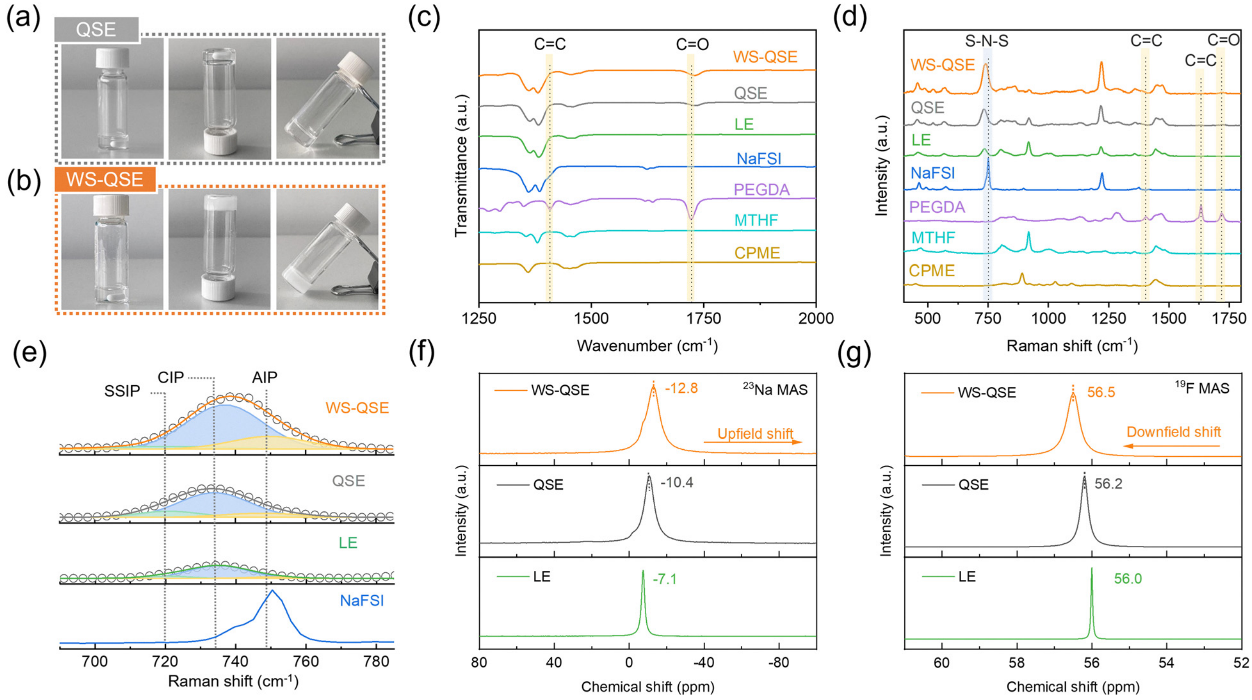

Fig. 3 (a) QSE and (b) WS-QSE shown as liquid precursors before polymerization (left) and after *in situ* polymerization (middle and right). (c) ATR-FTIR and (d) Raman spectroscopy characterization of WS-QSE, QSE, LE, NaFSI, PEGDA, MTHF, and CPME. (e) Raman spectra in the range of 710–780 cm^{-1} for WS-QSE, QSE, LE, and NaFSI. MAS solid-state NMR analysis (f) ^{23}Na and (g) ^{19}F spectra.

Na^+ is surrounded by seven Lewis basic centers (Fig. S8c). The additional upfield shift observed for WS-QSE indicates a stronger Na^+–anion interaction as promoted by the weakly solvating solvent.[45]

Complementary ^{19}F MAS spectra (Fig. 3g and Fig. S8b) revealed a consistent pattern, with WS-QSE showing the highest downfield shifts (56.5 ppm) compared to QSE (56.2 ppm) and LE (56.0 ppm). These shifts are similar to the mean ^{19}F chemical shift (56.8 ppm) observed in crystalline NaFSI (Fig. S8b) and suggest predominantly chelating coordination of FSI^-. The decreased electron shielding around fluorine atoms in WS-QSE suggests a stronger interaction between Na^+ and FSI^- there compared to LE and QSE.[18,46] The near-zero ^{19}F chemical-shift anisotropies demonstrate that the FSI^- anion reoriented rapidly and isotropically, despite confinement within the PEGDA matrix. These NMR analyses align well with our experimental observations from Raman spectroscopy (Fig. 3d and e) and computational findings from MD simulation (Fig. 2c–h), providing further evidence for an anion-dominated solvation structure in WS-QSE.

Electrochemical performance and SEI characterization of WS-QSE

Based on our understanding of the physicochemical and solvation properties of WS-QSE, we conducted a comprehensive array of electrochemical tests. Linear sweeping voltammetry (LSV) measurements using a Na|carbon-coated aluminum (Al) cell, revealed the superior electrochemical stability of WS-QSE, with an onset potential of 4.17 V *vs.* Na^+/Na at a 0.01 mA cm^{-2} cutoff,[53,54] compared to QSE (3.9 V), and LE (3.8 V) (Fig. 4a). According to the literature, the enhanced stability can be attributed to the improved anodic resistance of the cross-linked PEGDA backbone[48] and the cyclopentyl group of CPME.[30] To assess this enhanced anodic stability, we evaluated the electrolytes using a $Na_3V_2(PO_4)_3$ cathode, which operates between 2.4 and 3.8 V (*vs.* Na^+/Na) as shown in Fig. S9. Notably, WS-QSE (Fig. S9c and d) demonstrated improved stability at higher voltage than LE (Fig. S9a) and QSE (Fig. S9b). Cyclic voltammetry (CV) test, which was used to assess cathodic stability, indicated that both WS-QSE and QSE exhibited PEGDA reduction peaks at $\sim$0.76 V,[55] while LE exhibited no such reduction peak (Fig. S10). WS-QSE demonstrated a gradual increase in current over cycling, indicating improved Na^+ reversibility and stable SEI formation. In contrast, QSE and LE exhibited a rapid increase in current, suggesting uncontrolled decomposition. These results imply that WS-QSE has better electrochemical stability at both cathodic and anodic potentials. The CEs of the electrolytes were studied using Na|carbon-coated Al half-cells, as shown in Fig. 4b, where WS-QSE maintained an average CE of 97.9% over 300 cycles, significantly outperforming both LE (94.5%) and QSE (81.0%) at 0.2 mA cm^{-2} and 0.2 mAh cm^{-2}. Experimental optimization of the MTHF : CPME ratio revealed peak performance at a 50 : 50 volume ratio, achieving a CE of 98.4% over 400 cycles at increased cycling parameters (0.5 mA cm^{-2} and 0.5 mAh cm^{-2}) (Fig. 4c and Fig. S11a). At double the current and capacity densities (1 mA cm^{-2}, 1 mAh cm^{-2}), the Na|WS-QSE|carbon-coated Al cells maintained an average CE of 95.3% over 50 cycles (Fig. S11b). The cell also showed stable cycling performance at higher capacity densities of 3 mAh cm^{-2}, confirming the robustness of the WS-QSE electrolyte under demanding operational conditions (Fig. S11c). Additionally, a modified Aurbach's CE test[56,57] (detailed conditions are provided in the Methods section) with a limited Na reservoir (2 mAh cm^{-2}) showed that WS-QSE achieved a CE of 94.5%, while LE failed due to short-circuiting and QSE exhibited only 40.0% efficiency (Fig. 4d).

Symmetrical cells were examined to understand the stability of the Na/electrolyte interphase. As shown in Fig. 4e, WS-QSE demonstrated exceptional longevity, maintaining stability for 800 hours compared to QSE (350 hours) and LE (80 hours) in Na|Na cells, at a current density of 0.05 mA cm^{-2} with matched capacity density. This superior performance was achieved despite a slightly higher overpotential (0.1 V *vs.* Na^+/Na) due to lower ionic conductivities (0.28 mS cm^{-1}) for WS-QSE (Fig. S12), a characteristic trade-off noted in electrolytes with low solvating power.[29,30] Optimizing ionic conductivity was beyond the scope of this work. However, it presents a clear avenue for future research through the inclusion of strongly solvating additives[58] or modifications to the polymer backbone.

When the current density was increased from 0.01 to 1 mA cm^{-2} (Fig. 4f), WS-QSE maintained stable performance. In contrast, LE and QSE failed at much lower current densities (0.2 and 0.5 mA cm^{-2}, respectively). This improved rate performance was observed at higher current and capacity densities (0.5 mA cm^{-2} and 0.5 mAh cm^{-2}) as illustrated in Fig. S13a, and further confirmed under more demanding conditions of 1.0 mA cm^{-2} and 1.0 mAh cm^{-2}, where WS-QSE consistently cycled for 40 hours, while QSE and LE failed within 3 hours and 1 hour, respectively (Fig. S13b–d). Surface characterization revealed the mechanisms underlying the enhanced performance of WS-QSE. As shown in Fig. 4g, scanning electron microscopy (SEM) analysis of the Na–metal anode surface after 130 hours of cycling demonstrated that WS-QSE produced a compact and uniform surface structure, indicating stable SEI formation. In contrast, QSE resulted in a loosely structured surface, while LE produced a porous and pulverized surface morphology, suggesting less effective surface protection. X-ray photoelectron spectroscopy (XPS) analysis provided insights into the SEI composition (Fig. 4h, i, and Fig. S14). Analysis of the F1s spectra (Fig. 4h) revealed characteristic peaks at 687 and 684 eV, corresponding to S–F and NaF bonds, respectively,[59] resulting from NaFSI decomposition. Notably, both WS-QSE and QSE exhibited significantly stronger NaF (684 eV) signals compared to LE, indicating the enhanced reduction of Na^+–FSI^- complexes. This finding is consistent with their anion-dominated solvation structures previously observed through Raman spectroscopy (Fig. 3d, e and Fig. S7) and MD simulations (Fig. 2c–h). The abundance of NaF is particularly beneficial, as it has been reported to suppress Na dendrite growth and prolong the lifespan of the Na–metal anode.[8,13] Further analysis of the N1s spectra (Fig. 4i) revealed additional insights into the interphase composition. Both WS-QSE and QSE showed two distinct peaks,

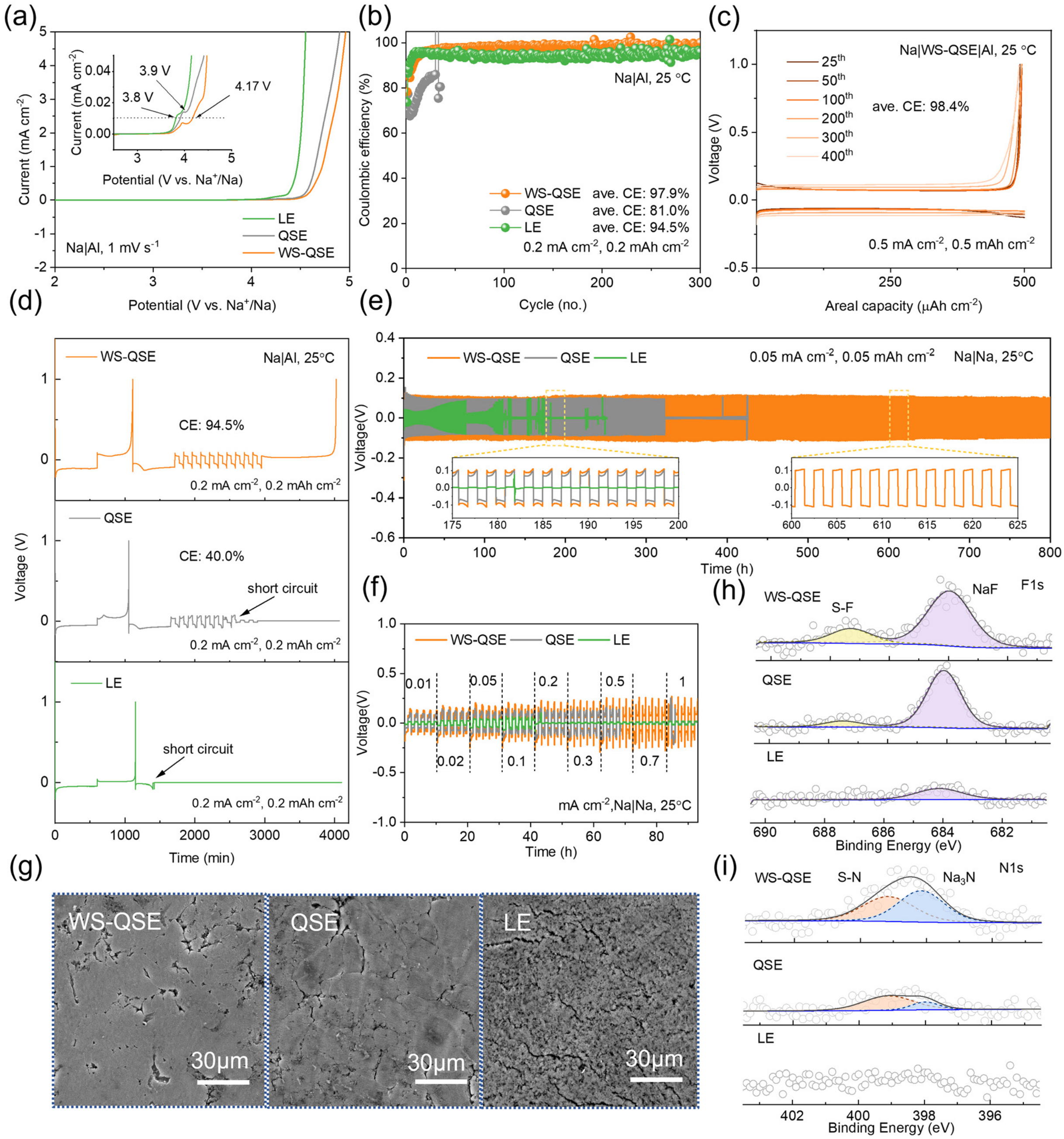

Fig. 4 (a) LSV curves of Na|carbon-coated Al cells using LE, QSE, and WS-QSE. (b) Average CE from the Na reversibility test for Na|carbon-coated Al cells utilizing LE, QSE, and WS-QSE at 0.2 mA cm^{-2} and 0.2 mAh cm^{-2} over 300 cycles. (c) Average CE for Na|WS-QSE|carbon-coated Al cells at 0.5 mA cm^{-2} and 0.5 mAh cm^{-2} for 400 cycles. (d) Modified Aurbach's CE test of Na|carbon-coated Al cells using LE, QSE, and WS-QSE at 0.2 mA cm^{-2} and 0.2 mAh cm^{-2}. Stripping and plating tests of Na|Na symmetric cells using LE, QSE, and WS-QSE were conducted (e) at 0.05 mA cm^{-2} and 0.05 mAh cm^{-2}; and (f) with stepwise increasing current densities from 0.01 to 1 mA cm^{-2} and from 0.01 to 1 mAh cm^{-2}. (g) SEM images of Na deposition on the Na–metal anode in Na|Na symmetric cells using LE, QSE, and WS-QSE after 130 hours. XPS analysis of cycled Na|Na symmetric cells with LE, QSE, and WS-QSE includes the (h) F 1s and (i) N 1s spectra.

namely S–N (399 eV) and Na_3N (398 eV),[9] which also originate from NaFSI decomposition. The presence of Na_3N is particularly significant as it promotes rapid Na^+ diffusion through the SEI and uniform Na deposition.[17,60,61] Furthermore, its high mechanical strength (shear modulus: 23.95 GPa)[62] is crucial for suppressing dendritic growth. When combined with the robust NaF (shear modulus: 31.4 GPa),[63] this creates a composite inorganic SEI that simultaneously delivers fast ionic transport, mechanical stability, and dendrite suppression.[61,63] The more pronounced Na_3N signal observed in WS-QSE directly correlates with its superior rate performance and extended cycling stability observed in symmetrical cell tests, providing compelling evidence that our solvation structure design strategy effectively promotes the formation of a favorable SEI.

Performance of WS-QSE in room temperature Na/SPAN batteries

To demonstrate the practical significance of our electrolyte design strategy, we evaluated the WS-QSE system in Na/sulfur batteries using SPAN as the positive electrode. SPAN offers several key advantages, including a high theoretical capacity for sulfur (1675 mAh g^{-1}), good structural stability through covalent sulfur–polyacrylonitrile bonds[13,43,44] and an operating voltage range (0.8–3 V) that aligns well with the stability window of WS-QSE. The XRD pattern of the as-prepared SPAN is shown in Fig. S15, with its detailed preparation outlined in the Methods section. Initial CV testing at 0.1 mV s^{-1} revealed a significant difference in performance between the electrolyte systems.[64] As illustrated in Fig. 5a and Fig. S16, the Na|LE|-SPAN cells exhibited signs of short-circuiting at approximately 1.8 V during the anodic scanning, likely due to instability at the moderate sweep rate. In contrast, the WS-QSE system showed excellent stability with overlapping CV profiles in the first three cycles (Fig. S16).

Cycling stability tests further validated the advantages of WS-QSE. After three formation cycles at 120 mA g^{-1}, the cells were cycled at 240 mA g^{-1}. As shown in Fig. 5b and Fig. S17, the WS-QSE system sustained a capacity of 1079 mAh g^{-1} over 100 cycles, significantly outperforming both the QSE (936 mAh g^{-1}) and LE systems, with the latter failing within five cycles. This improved stability can be attributed to the protective PEGDA framework and the robust SEI formation previously characterized (Fig. 4g–i).

Post-cycling XPS analysis was used to provide key insights into the cathode-electrolyte interface (CEI) in a fully charged state (Fig. S18 and SI II). While both the WS-QSE (Fig. S18d) and QSE (Fig. S18c) systems showed signs of PEGDA backbone decomposition as indicated by strong C═O intensities, the LE system exhibited high levels of SO_x–F and C–S/C–S species (Fig. S18b), indicating that uncontrolled NaFSI salt decomposition formed an ineffective CEI. Importantly, all systems showed the presence of NaF, which helps suppress polysulfide dissolution.[21] The absence of Na_2S (~160 eV)[15,21] in all

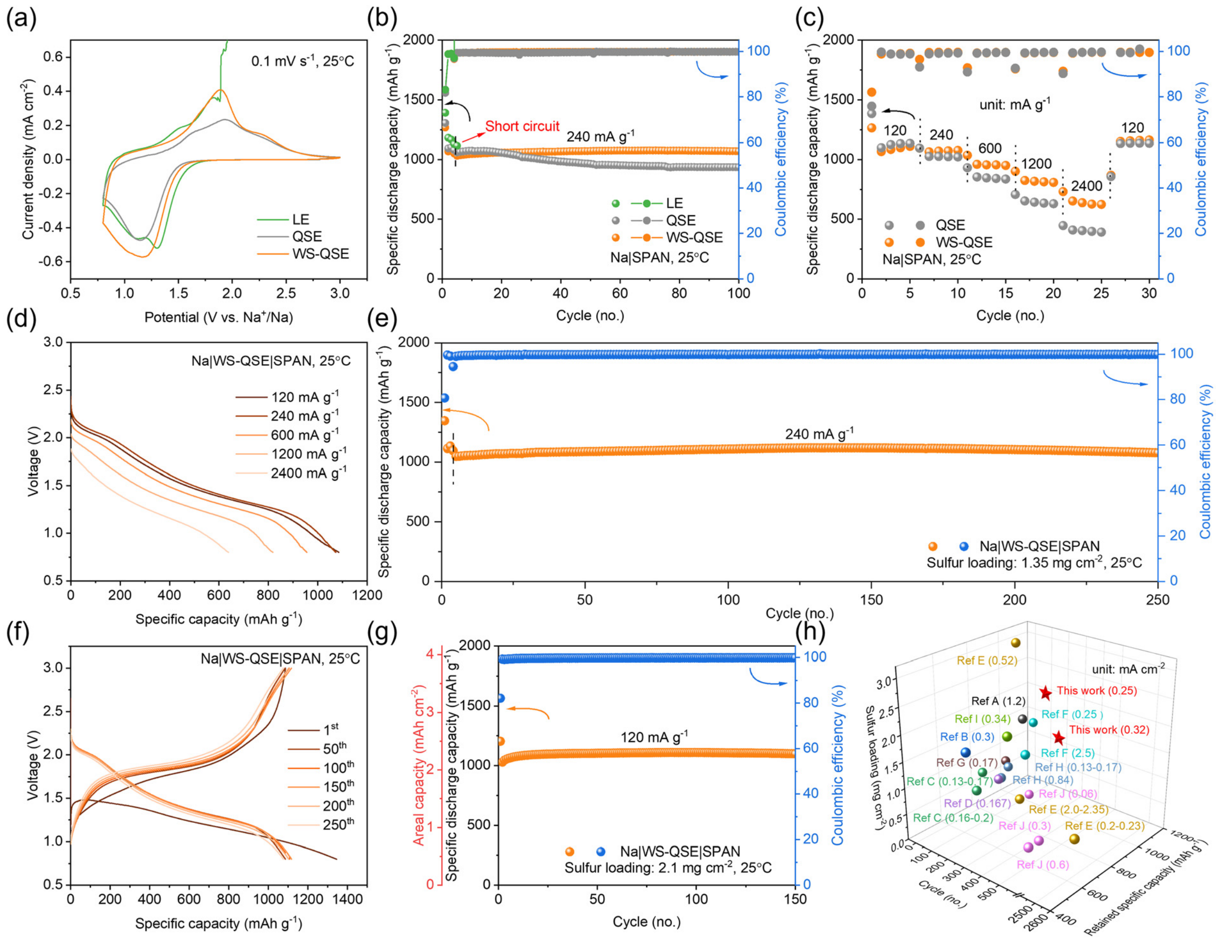

Fig. 5 (a) CV curves of Na|SPAN cells using LE, QSE, and WS-QSE at 0.1 mV s^{-1} and 25 °C. (b) Cycling stability and CE of Na|SPAN cells utilizing LE, QSE, and WS-QSE at a charge–discharge rate of 240 mA g^{-1} within the voltage range of 0.8–3 V at 25 °C. (c) Rate capability testing of the Na|WS-QSE|SPAN and Na|QSE|SPAN batteries at 25 °C. (d) Discharge curves of Na|WS-QSE|SPAN at various rates. (e) Cycling tests of Na|WS-QSE|SPAN cells with a sulfur loading of 1.35 mg cm^{-2} at 240 mA g^{-1} and 25 °C; (f) corresponding charge–discharge curves. (g) Cycling tests of the Na|WS-QSE|SPAN cell with a sulfur loading of 2.1 mg cm^{-2}, an areal capacity of 2.3 mAh cm^{-2} at 120 mA g^{-1} (or 0.25 mA cm^{-2}), and 25 °C. (h) Retained Na|WS-QSE|SPAN battery capacity compared to previously reported room temperature Na/sulfur batteries across various cycle numbers and sulfur loadings.

electrolytes (Fig. S18b–d) suggests that the electrochemical reactions remained largely reversible for the SPAN cathode. This finding provides support that the rapid failure of the LE-based cell originates not from the cathode, but from the inherent instability of the Na anode.

XPS depth profiling analysis was used to demonstrate that the SEI thickness follows the order WS-QSE $\geq$ QSE $>$ LE (Fig. S19 and S20 with detailed discussion provided in SI III), with WS-QSE maintaining both stable C1s and F1s signals throughout 30 minutes of sputtering, compared to the rapid signal decay in LE and QSE. The superior interfacial stability of the WS-QSE is attributed to its protective role of PEGDA and the formation of a more uniform SEI layer (Fig. S19 and S20 and Fig. 4g), both factors leading to improved cycling stability with reduced capacity fade.

The rate capability testing revealed an interesting performance tradeoff. As illustrated in Fig. 5c and d and Fig. S21, the batteries with QSE exhibited marginally higher capacity (1134 mAh g^{-1} *vs.* 1097 mAh g^{-1}) at low rates (120 mA g^{-1}) due to its superior ionic conductivity (Fig. S12). However, the WS-QSE batteries demonstrated a better capacity retention at higher rates, maintaining 634 mAh g^{-1} at 2400 mA g^{-1}, compared to QSE's 404 mAh g^{-1}. This enhanced rate performance correlates directly with the NaF and Na_3N-rich interphase structure identified by XPS analysis (Fig. 4h and i).

Most significantly, long-term testing with sulfur loadings of 1.35 mg cm^{-2} further supported the stability of WS-QSE. As illustrated in Fig. 5e and f, the WS-QSE had excellent cycling stability, maintaining a capacity of 1077 mAh g^{-1} (484.7 mAh $g_{SPAN}{}^{-1}$) over 250 cycles at 240 mA g^{-1} (or 0.32 mA cm^{-2}). Even more impressively, at a higher sulfur loading of 2.1 mg cm^{-2}, the cells sustained 1099 mAh g^{-1} (494.6 mAh $g_{SPAN}{}^{-1}$) over 150 cycles, achieving a high areal capacity of 2.3 mAh cm^{-2} at 120 mA g^{-1} (or 0.25 mA cm^{-2}), as shown in Fig. 5g. These results surpass previously reported room temperature Na/sulfur batteries in both loading and capacity retention (Fig. 5h and Table S2),[11–13,15,17,18,32,39,45,60,65] To demonstrate its practical applicability, we tested the WS-QSE in full cells with limited-excess Na anodes prepared by two different methods. Anodes prepared by mechanical rolling (N/P ratio = 6.7 : 1, Fig. S22) retained a capacity of 1031 mAh g^{-1} after 20 cycles. Those prepared by electrodeposition (N/P ratio = 3 : 1, Fig. S23) retained 780 mAh g^{-1} over the same period. These results confirm the robustness of the WS-QSE electrolyte system under practical conditions with lower Na excess (Fig. S22 and S23).

Conclusions

This work establishes a novel electrolyte design framework for NMBs through manipulation of Na^+ solvation environment, demonstrating how weakly solvating solvents combined with polymer matrices can create anion-derived interfaces that dramatically enhance battery performance and stability. Through the incorporation of CPME as a weakly solvating co-solvent within the QSE framework, combined with the utilization of PEGDA's carboxyl groups to reduce Na^+–solvent interactions, we engineered an electrolyte system that promotes predominant anion coordination around Na^+ ions, creating the desired anion-dominated solvation environment. Through computations and characterizations using MD simulations, Raman spectroscopy, solid-state NMR spectroscopy, and XPS analysis, we demonstrated that the interplay among salt, solvent, and polymer components leads to a favorable anion-derived SEI at the Na–metal surface. The system achieves high CE over 400 cycles in half-cell tests, and a capacity retention of 1099 mAh g^{-1} in practical Na-sulfur batteries with high sulfur loading (2.1 mg cm^{-2}). Beyond these immediate performance improvements, this novel methodology advances NMBs technology and establishes a new paradigm for electrolyte design in next-generation energy storage systems.

Author contributions

H. M. L. and F. C. conceived the idea. H. M. L. designed and performed the experiments, basic characterizations, formal analysis, and DFT calculations. Z. W. performed the molecular dynamics simulations and wrote the computational details. S. X. helped with the investigation. R. S. conducted the NMR experiment. Q. W. provided the electrode materials. Z. W., S. X., L. S., B. P., Y. W., R. S., J. S., Q. W., and F. C. provided valuable feedback and facilitated the systematic analysis of data. H. M. L. and F. C. wrote the manuscript. All authors revised and reviewed the manuscript. F. C. and Q. W. oversaw the research. F. C. supervised the project.

Conflicts of interest

There are no conflicts to declare.

Data availability

Original data are available from the corresponding authors upon reasonable request. The data suppoting this article have been included as part of the supplementary information, which includes methods, calculations, figures (Fig. S1–S23), tables (Tables S1 and S2), and additional references. See DOI: **https://doi.org/10.1039/d5ee02153g**.

Acknowledgements

Support from the BayBatt Cell Technology Center is gratefully acknowledged, funded by the Deutsche Forschungsgemeinschaft (DFG, German Research Foundation) - INST 91/452-1 LAGG. The project was also funded by the Deutsche Forschungsgemeinschaft (DFG, German Research Foundation) 533115776. FC thanks the University of Bayreuth and the Bavarian Center for Battery Technology (BayBatt) for providing start-up funds. The authors thank Ms. Beate Bojer for collecting the multinuclear MAS NMR spectra using the NMR facilities of the Northern Bavaria NMR Center (NBNC) at the University of Bayreuth. The authors thank Prof. Dr. Seema Agarwal for her technical support. Dr. B. Py thanks the

Hong Kong PhD Fellowship Scheme for its financial support. The authors also thank Mr. Berk Oğuz for assistance.

References

1 C. Vaalma, D. Buchholz, M. Weil and S. Passerini, *Nat. Rev. Mater.*, 2018, **3**, 18013.
2 L. Chen, M. Fiore, J. E. Wang, R. Ruffo, D. K. Kim and G. Longoni, *Adv. Sustainable Syst.*, 2018, **2**, 1700153.
3 K. Chayambuka, G. Mulder, D. L. Danilov and P. H. L. Notten, *Adv. Energy Mater.*, 2018, **8**, 1800079.
4 B. Lee, E. Paek, D. Mitlin and S. W. Lee, *Chem. Rev.*, 2019, **119**, 5416–5460.
5 C. Bao, B. Wang, P. Liu, H. Wu, Y. Zhou, D. Wang, H. Liu and S. Dou, *Adv. Funct. Mater.*, 2020, **30**, 2004891.
6 M. Hou, Y. Zhou, F. Liang, H. Zhao, D. Ji, D. Zhang, L. Li and Y. Lei, *Chem. Eng. J.*, 2023, **475**, 146227.
7 Y. Jin, P. M. L. Le, P. Gao, Y. Xu, B. Xiao, M. H. Engelhard, X. Cao, T. D. Vo, J. Hu, L. Zhong, B. E. Matthews, R. Yi, C. Wang, X. Li, J. Liu and J.-G. Zhang, *Nat. Energy*, 2022, **7**, 718–725.
8 H. M. Law, J. Yu, S. C. T. Kwok, G. Zhou, M. J. Robson, J. Wu and F. Ciucci, *Energy Storage Mater.*, 2022, **46**, 182–191.
9 J. Yu, W. Ren, C. Yu, Z. Wang, Y. Xie and J. Qiu, *Energy Environ. Mater.*, 2023, **6**, e12602.
10 E. Park, J. Park, K. Lee, Y. Zhao, T. Zhou, G. Park, M.-G. Jeong, M. Choi, D.-J. Yoo, H.-G. Jung, A. Coskun and J. W. Choi, *ACS Energy Lett.*, 2022, **8**, 179–188.
11 Y. Ren, T. Lai and A. Manthiram, *ACS Energy Lett.*, 2023, **8**, 2746–2752.
12 D. Liu, Z. Li, X. Li, X. Chen, Z. Li, L. Yuan and Y. Huang, *ACS Appl. Mater. Interfaces*, 2022, **14**, 6658–6666.
13 J. Wu, J. Liu, Z. Lu, K. Lin, Y.-Q. Lyu, B. Li, F. Ciucci and J.-K. Kim, *Energy Storage Mater.*, 2019, **23**, 8–16.
14 A. C. Thenuwara, P. P. Shetty, N. Kondekar, C. Wang, W. Li and M. T. McDowell, *J. Mater. Chem. A*, 2021, **9**, 10992–11000.
15 X. Xu, D. Zhou, X. Qin, K. Lin, F. Kang, B. Li, D. Shanmukaraj, T. Rojo, M. Armand and G. Wang, *Nat. Commun.*, 2018, **9**, 3870.
16 W. Fang, H. Jiang, Y. Zheng, H. Zheng, X. Liang, Y. Sun, C. Chen and H. Xiang, *J. Power Sources*, 2020, **455**, 227956.
17 J. He, A. Bhargav, W. Shin and A. Manthiram, *J. Am. Chem. Soc.*, 2021, **143**, 20241–20248.
18 D. Guo, J. Wang, T. Lai, G. Henkelman and A. Manthiram, *Adv. Mater.*, 2023, **35**, e2300841.
19 M. S. Kim, Z. Zhang, P. E. Rudnicki, Z. Yu, J. Wang, H. Wang, S. T. Oyakhire, Y. Chen, S. C. Kim, W. Zhang, D. T. Boyle, X. Kong, R. Xu, Z. Huang, W. Huang, S. F. Bent, L. W. Wang, J. Qin, Z. Bao and Y. Cui, *Nat. Mater.*, 2022, **21**, 445–454.
20 F. Huang, P. Xu, G. Fang and S. Liang, *Adv. Mater.*, 2024, **36**, e2405310.
21 K. Liao, M. H. Pai and A. Manthiram, *Adv. Energy Mater.*, 2024, **15**, 2403733.
22 Z. Lin, Y. Wang, Y. Li, Y. Liu, S. Zhong, M. Xie, F. Yan, Z. Zhang, J. Peng, J. Li, A. Wang, X. Chen, M. Zhai, H. Zhang and J. Qiu, *Energy Storage Mater.*, 2022, **53**, 917–926.
23 C. Zheng, J. Wu, L. Zhang and H. Wang, *J. Mater. Chem. C*, 2023, **11**, 344–363.
24 Y.-X. Yao, X. Chen, C. Yan, X.-Q. Zhang, W.-L. Cai, J.-Q. Huang and Q. Zhang, *Angew. Chem., Int. Ed.*, 2021, **60**, 4090–4097.
25 H. Fang, Y. Huang, W. Hu, Z. Song, X. Wei, J. Geng, Z. Jiang, H. Qu, J. Chen and F. Li, *Angew. Chem., Int. Ed.*, 2024, **63**, e202400539.
26 S. Wang, X. G. Zhang, Y. Gu, S. Tang and Y. Fu, *J. Am. Chem. Soc.*, 2024, **146**, 3854–3860.
27 Y. Liao, M. Zhou, L. Yuan, K. Huang, D. Wang, Y. Han, J. Meng, Y. Zhang, Z. Li and Y. Huang, *Adv. Energy Mater.*, 2023, **13**, 2301477.
28 H. Lu, Q. Wang, J. Chen, H. Zhang, J. Ding, Y. Nuli, J. Yang and J. Wang, *Energy Storage Mater.*, 2023, **63**, 102994.
29 T. Ma, Y. Ni, D. Li, Z. Zha, S. Jin, W. Zhang, L. Jia, Q. Sun, W. Xie, Z. Tao and J. Chen, *Angew. Chem., Int. Ed.*, 2023, **62**, e202310761.
30 H. Zhang, Z. Zeng, F. Ma, Q. Wu, X. Wang, S. Cheng and J. Xie, *Angew. Chem., Int. Ed.*, 2023, **62**, e202300771.
31 C. Yang, S. Xin, L. Mai and Y. You, *Adv. Energy Mater.*, 2020, **11**, 2000974.
32 S. Murugan, S. V. Klostermann, P. Schützendübe, G. Richter, J. Kästner and M. R. Buchmeiser, *Adv. Funct. Mater.*, 2022, **32**, 2201191.
33 X. Zhou, Z. Li, W. Li, X. Li, J. Fu, L. Wei, H. Yang and X. Guo, *Adv. Funct. Mater.*, 2022, **33**, 2212866.
34 W. Zhang, J. Zhang, X. Liu, H. Li, Y. Guo, C. Geng, Y. Tao and Q. H. Yang, *Adv. Funct. Mater.*, 2022, **32**, 2201205.
35 X. Judez, M. Martinez-Ibañez, A. Santiago, M. Armand, H. Zhang and C. Li, *J. Power Sources*, 2019, **438**, 226985.
36 X. He, Y. Ni, Y. Hou, Y. Lu, S. Jin, H. Li, Z. Yan, K. Zhang and J. Chen, *Angew. Chem., Int. Ed.*, 2021, **60**, 22672–22677.
37 G. Zhou, J. Yu, J. Liu, X. Lin, Y. Wang, H. M. Law and F. Ciucci, *Cell Rep. Phys. Sci.*, 2022, **3**, 100722.
38 Z. Wang, Y. Wang, L. Shen, Z. Jin, H. M. Law, A. Wang, W. Wang and F. Ciucci, *Energy Environ. Sci.*, 2023, **16**, 4084–4092.
39 D. Zhou, Y. Chen, B. Li, H. Fan, F. Cheng, D. Shanmukaraj, T. Rojo, M. Armand and G. Wang, *Angew. Chem., Int. Ed.*, 2018, **57**, 10168–10172.
40 J. Ma, M. Yu, M. Huang, Y. Wu, C. Fu, L. Dong, Z. Zhu, L. Zhang, Z. Zhang, X. Feng and H. Xiang, *Small*, 2024, **20**, e2305649.
41 J. Ma, X. Feng, Y. Wu, Y. Wang, P. Liu, K. Shang, H. Jiang, X. Hou, D. Mitlin and H. Xiang, *J. Energy Chem.*, 2023, **77**, 290–299.
42 H. V. Ramasamy, S. Kim, E. J. Adams, H. Rao and V. G. Pol, *Chem. Commun.*, 2022, **58**, 5124–5127.
43 M. S. Syali, D. Kumar, K. Mishra and D. K. Kanchan, *Energy Storage Mater.*, 2020, **31**, 352–372.
44 S. Tan, M. M. Rahman, Z. Wu, H. Liu, S. Wang, S. Ghose, H. Zhong, I. Waluyo, A. Hunt, P. Liu, X.-Q. Yang and E. Hu, *ACS Energy Lett.*, 2023, **8**, 2496–2504.
45 M. H. Pai, T. Lai and A. Manthiram, *Adv. Funct. Mater.*, 2024, **34**, 2407450.
46 Z. Li, H. Rao, R. Atwi, B. M. Sivakumar, B. Gwalani, S. Gray, K. S. Han, T. A. Everett, T. A. Ajantiwalay, V. Murugesan, N. N. Rajput and V. G. Pol, *Nat. Commun.*, 2023, **14**, 868.

47 T. D. Pham and K. K. Lee, *Small*, 2021, **17**, e2100133.
48 Q. Lu, C. Wang, D. Bao, H. Duan, F. Zhao, K. Doyle-Davis, Q. Zhang, R. Wang, S. Zhao, J. Wang, H. Huang and X. Sun, *Energy Environ. Mater.*, 2023, **6**, e12447.
49 J. Zhu, C. Kang, S. Mo, Y. Zhang, X. Xiao, F. Kong and G. Yin, *ChemSusChem*, 2023, **16**, e202202060.
50 X. Peng, T. Wang, B. Liu, Y. Li and T. Zhao, *Energy Environ. Sci.*, 2022, **15**, 5350–5361.
51 L. Chen, Q. Zhang, C. Song, Y. Jiang, X. Sheng, H. Pan, L. Yang, S. Wu, L. Zeng, D. Sun, C. Wang, T. Wang, Y. Li and T. Zhao, *Angew. Chem., Int. Ed.*, 2025, **64**, e202422791.
52 X. Chen, H. R. Li, X. Shen and Q. Zhang, *Angew. Chem., Int. Ed.*, 2018, **57**, 16643–16647.
53 H. Wang, T. Liu, X. Du, J. Wang, Y. Yang, H. Qiu, G. Lu, H. Li, Z. Chen, J. Zhao and G. Cui, *Batteries Supercaps*, 2022, **5**, e202200246.
54 Z. Li, Y. Zhao and W. E. Tenhaeff, *ACS Appl. Energy Mater.*, 2019, **2**, 3264–3273.
55 C. Piedrahita, V. Kusuma, H. B. Nulwala and T. Kyu, *Solid State Ion.*, 2018, **322**, 61–68.
56 Y. Deng, S. Feng, Z. Deng, Y. Jia, X. Zhang, C. Xu, S. Miao, M. Yao, K. Wu, Y. Zhang and W. Cai, *J. Energy Chem.*, 2023, **87**, 105–113.
57 Y. Zou, B. Zhang, H. Luo, X. Yu, M. Yang, Q. Zheng, J. Wang, C. Jiao, Y. Chen, H. Zhang, J. Xue, X. Kuai, H. G. Liao, C. Ouyang, Z. Ning, Y. Qiao and S. G. Sun, *Adv. Mater.*, 2024, **36**, e2410261.
58 Z. Wang, T. Zheng, S. Wang, X. G. Zhang, Y. Gu, S. Tang and Y. Fu, *J. Am. Chem. Soc.*, 2025, **147**, 5962–5970.
59 G. G. Eshetu, T. Diemant, M. Hekmatfar, S. Grugeon, R. J. Behm, S. Laruelle, M. Armand and S. Passerini, *Nano Energy*, 2019, **55**, 327–340.
60 J. Wu, Y. Tian, Y. Gao, Z. Gao, Y. Meng, Y. Wang, X. Wang, D. Zhou, F. Kang, B. Li and G. Wang, *Angew. Chem., Int. Ed.*, 2022, **61**, e202205416.
61 W. Tian, G. Lin, S. Yuan, T. Jin, Q. Wang and L. Jiao, *Angew. Chem., Int. Ed.*, 2025, **64**, e202423075.
62 M. Yang, X. Chang, L. Wang, X. Wang, M. Gu, H. Huang, L. Tang, Y. Zhong and H. Xia, *Adv. Mater.*, 2023, **35**, e2208705.
63 S. Kim, Y. Jung, J. Park, M. Hong and H. R. Byon, *Bull. Korean Chem. Soc.*, 2021, **42**, 1519–1523.
64 X. Huang, Z. Wang, R. Knibbe, B. Luo, S. A. Ahad, D. Sun and L. Wang, *Energy Technol.*, 2019, **7**, 1801001.
65 T. Zhu, X. Dong, Y. Liu, Y.-G. Wang, C. Wang and Y.-Y. Xia, *ACS Appl. Energy Mater.*, 2019, **2**, 5263–5271.